

Estimation of Net Photosynthetically Available Radiation Over Oceans from Satellite Data: Application to a Dynamical Model of a Plankton Bloom in the Atlantic Ocean*

Abstract

A radiative transport model has been developed for the simulation of photosynthetically available radiation (PAR) flux density transfer in clear and cloudy atmospheres. Vertical profiles of temperature, pressure, and atmospheric constituents by globally distributed radiosonde measurements with multiple cloud layers of different types and fractional coverages are used to represent the natural variability of clear and cloudy atmospheres. A multivariate analysis for the parameterization of (net) surface PAR flux densities as a function of the solar elevation and the system reflectivity measurable by satellite sensors was carried out. The resulting retrievals show standard errors less than 35 Wm^{-2} for cloudy scenes and 5 Wm^{-2} for clear skies. The regression algorithms were applied to NOAA AVHRR satellite measurements and compared to simultaneously recorded shipborne data logs during a cruise of the UK research vessel *Charles Darwin* in May 1990 in the north Atlantic. The impact of the satellite net PAR maps on two-dimensional (2D) dynamical phytoplankton modeling is described.

Introduction

The matter and energy exchange in the marine biosphere and the corresponding fluxes across the sea surface are essentially influenced by the amount of photosynthetically available radiation (PAR) (e.g., Platt *et al.*, 1989; Sathyendranath and Platt, 1988). The annual phytoplankton growth cycle depends on the effectivity of photosynthesis; thus, the availability of light with wavelengths between 300 nm and 700 nm plays a key role for global biosphere-atmosphere interactions. Because the coverage of coastal or shipborne stations measuring surface PAR irradiances on a global and continuous scale is limited, satellite data and appropriate methods to de-

rive the relevant parameters from the radiometric measurements are required.

For climatic applications, i.e., surface radiation budget observations, satellite data are operationally used mainly for the analyses of spectrally broadband sensor measurements on geostationary platforms. Current programs (e.g., International Satellite Cloud Climatology Project (ISCCP)) provide global statistics of atmospheric and cloud properties and standardized models to compute the relevant surface parameters (Bishop and Rossow, 1991). In recent studies the PAR portion is generally calculated as a constant fraction of the global radiation (Jitts *et al.*, 1976), or simple parameterizations are found to derive the surface PAR irradiances restricted to cloudfree situations (Frouin *et al.*, 1989). Eck and Dye (1991) used the ultraviolet backscatter signal measured by the TOMS to estimate the potential clear sky irradiance which was then corrected for cloud effects by a linear relation.

Our approach provides a new technique to derive the downwelling PAR flux densities (i.e., irradiances) over oceans and the PAR net flux densities below the water surface for variable atmospheric and cloud conditions. Parameterizations are given for the PAR calculation by the use of the sun zenith angle and the hemispherical albedo computed from satellite reflectivity measurements in the visible wavelength interval between 500 nm and 700 nm. The algorithms are presented for three different PAR wavelength intervals which are commonly used and for cloudfree and cloudy cases, including partially cloud coverage. A case study is carried out for the comparison of preliminary application results to shipborne measurements during a Biogeochemical Ocean Flux Study (BOFS) cruise of the UK research vessel *Charles Darwin*. Finally, the potential implementation of the resulting PAR maps into two-dimensional (2D) phytoplankton models is shown to demonstrate the impact of spatial and temporal PAR supply on phytoplankton growth.

Simulations

Radiative Transport Model

Flux-type radiative transfer simulation models are generally used to calculate the up- and downwelling flux densities,

*Presented at the First Thematic Conference on Remote Sensing for Marine and Coastal Environments, New Orleans, Louisiana, 15-17 June 1992.

P. Bauer

Deutsche Forschungsanstalt für Luft- und Raumfahrt, Systemanalyse Raumfahrt, Cologne, Germany.

S. Gaito*, J. M. McGlade*, and D. Winter

Forschungszentrum Jülich, Arbeits-gruppe Theoretische Ökologie, Jülich, Germany.

*Presently with Ecosystems Analysis and Management Unit, Biological Sciences, University of Warwick, Coventry, United Kingdom.

Photogrammetric Engineering & Remote Sensing,
Vol. 59, No. 3, March 1993, pp. 323-329.

0099-1112/93/5903-323\$03.00/0

©1993 American Society for Photogrammetry
and Remote Sensing

i.e., hemispherically integrated radiation streams, at the boundaries of discrete atmospheric layers and the surface. These models have been proven as fast and accurate schemes in terms of energy budget calculations in stratified media. They are inappropriate for the investigation of exact radiation transport phenomena, in particular, if radiation intensities with angular resolution are required. The fundamental formulation of the downwelling PAR flux density at the surface, F_{PAR} , and the corresponding net flux density, $F_{PAR,net}$, as a function of the surface albedo, A_0 , the atmospheric transmission, τ_{PAR} , and the cosine of the sun zenith angle, μ_0 , is given by

$$F_{PAR} = S_{o,PAR} \mu_0 \tau_{PAR} \tag{1}$$

$$F_{PAR,net} = F_{PAR}(1 - A_0) = S_{o,PAR} \mu_0 \tau_{PAR,net} \tag{2}$$

where the transmission terms and the system albedo, ρ_{PAR} , can be defined as $\rho_{PAR} = F_{PAR} / S_{o,PAR}$, $\tau_{PAR,net} = F_{PAR,net} / S_{o,PAR}$, and $\rho_{PAR} = F_{r,PAR} / S_{o,PAR}$, respectively. $S_{o,PAR}$ denotes the solar irradiance at the top of the atmosphere and $F_{r,PAR}$ denotes the outward reflected flux density. The flux density amounts, transmissions, and the albedo have to be specified for the relevant spectral intervals. Here, they are computed for three wavelength bands which are generally used in biological assessments. The intervals and the values of the corresponding spectral solar irradiances are 300 nm to 700 nm (625 Wm^{-2}), 350 nm to 700 nm (585.6 Wm^{-2}), and 400 nm to 700 nm (530.3 Wm^{-2}), respectively. The basic differential equations of the model describe the dependence of the up- and downward flux densities of the direct (F^{dir}) and diffuse (F^{dif}) components at the layer boundaries on the optical properties of the layer (Zdunkowski *et al.*, 1980), and have to be calculated separately for cloudfree (*f*) and cloud covered (*c*) situations. For fractionally covered scenes the partial cloud coverage, *C*, is introduced, and the two parts are combined to

$$(F^{dir}, F^{dif}) = C(F^{dir}, F^{dif})_c + (1 - C)(F^{dir}, F^{dif})_f \tag{3}$$

For computational purposes, the atmosphere is subdivided into discrete layers, so that the above mentioned differential equations are computed iteratively for each layer and added to derive the total flux densities at the bottom and top of the atmosphere. Thus, horizontally and vertically inhomogeneous cloud and atmospheric structures are allowed in order to simulate the natural variability. The interaction of light in the PAR wavelength ranges with the atmospheric constituents are taken into account by parameterization schemes for ozone absorption (Lacis and Hansen, 1974), molecular scattering (Margaft and Griggs, 1969), and aerosol absorption and scattering (Coakley *et al.*, 1983). In cloudy cases, different cloud types are used as a function of cloud depth and base altitude, and their radiative properties are calculated using the δ -Eddington approximation of Joseph *et al.* (1976). The absorption of water vapor and other gases is generally negligible for wavelengths below 760 nm.

Model Atmospheres

The necessary input parameters are the vertical profiles of temperature, pressure, ozone and aerosol concentration, the cloud layer positions and types, the average cloud liquid water content, cloud fractional coverage, the surface hemispherical albedo, and the solar elevation angle. The temperature and pressure distributions with height were taken from profiles measured by globally distributed radiosonde ascents from experimental ship cruises during 1987-1989. The ozone concentrations were fitted to climatological profiles following the parametrization of Green (1964) with a randomly

varying total column and altitude of maximum concentration.

The aerosol concentration decreases exponentially with height, so that its variability was introduced by random variations of the surface concentration and the scale height, which is the altitude with 1/e of the surface concentration. Thus, total aerosol optical thicknesses between 0.1 and 0.5 occurred. A layer was classified as a cloud layer if the local relative humidity exceeded 98 percent.

The cloud optical properties are mainly a function of the cloud type, geometrical thickness, and horizontal coverage. The allowed types were Cumulus, Altostratus, Stratocumulus, Nimbostratus, and Stratus, respectively, with average liquid water contents between 0.25 gm^{-3} (Ns) and 0.95 gm^{-3} (Cu). The actually used water contents were derived by an additional random variation. The cloud coverage was separately defined for each cloud layer. The multivariate analyses included two types of random variations, i.e., equally distributed values limited by the specific minimum and maximum amounts, and normally distributed values determined by the sample average and the corresponding standard deviation. The key parameters and their variation ranges are given in Table 1.

By varying the described parameters once per atmospheric case and running the model for five randomly chosen solar zenith angles, a set of 1700 samples was generated for clear scenes and 1215 samples for cloudy cases. In Figure 1a the dependence of the PAR (300 to 700 nm) albedo and total transmission on the integrated optical depth is illustrated. The albedos reach maximum values of 0.8 for very dense clouds and nearly complete cloud coverages. The transmission drastically drops with increasing optical depth of the cloudy atmospheres, reaching nearly zero for values above 20 to 30. The large scatter is mainly produced by the variation in cloud coverage and sun elevation. Figure 1b shows the effect of the increasing optical depth on the direct and diffuse component of the downwelling flux densities. For low cloud amounts, the direct part dominates due to the small attenuation by droplet scattering. With increasing cloud depths, the direct transmission decreases exponentially and the diffuse part reaches a maximum for depths between 5 and 8. For optical thicknesses above 10, the irradiance is mainly diffuse.

Retrievals

With the simulated radiation flux densities as functions of the above given variable parameters, the basic data set for the retrieval analyses was given. To apply a multilinear regression, the relation between the desired variables and the free parameters have to be linearized. Additionally, the data must be equally distributed over the range of the retrieved flux densities in order to avoid inhomogeneous weights. The only

TABLE 1. PARAMETERS AND RANGES USED IN THE MULTIVARIATE ANALYSIS (*VALUES TAKEN FROM SILVERMAN AND SPRAGUE (1970)).

Parameter	Minimum	Maximum	Mean	Standard Deviation
O ₃ -Column	--	--	0.35 cm	0.05 cm
O ₃ -Maximum Height	20 km	25 km	--	--
Aerosol Scale Height	2 km	3 km	--	--
Aerosol Surface Extinction	0.01 km ⁻¹	0.02 km ⁻¹	--	--
Cloud LWC	--	--	Literature*	1/4 Literature*
Cloud Coverage	0.0	1.0	--	--
Surface Albedo	--	--	0.08	0.01
Solar Zenith Angle	0°	85°	--	--

regression parameters, which are accessible for satellite estimates without further informations about the atmospheric state, are the target reflectivity and the sun zenith angle. The conversion of the target reflectivity measured by the satellite sensor to the modeled hemispherical albedo, ρ^* , is given in the next section. The resulting equations for cloudfree conditions are

$$F_{PAR}, F_{PAR,net} = a_0 + a_1\mu_0 \quad (4a)$$

$$F_{PAR}, F_{PAR,net} = a_0 + a_1\mu_0 + a_2\mu_0^b \rho^{*c} \quad (4b)$$

with the retrieval coefficients a_i and the linearizing factors c and d . The first of Equations 4 denotes the retrieval without using the albedo, so that it is also applicable to independent surface estimations. The appropriate relations for cloudy cases are

$$F_{PAR}, F_{PAR,net} = a_0 + a_1\mu_0(1 - \rho^*) \quad (5a)$$

$$F_{PAR}, F_{PAR,net} = a_0 + a_1\mu_0 + a_2\mu_0(1 - \rho^{*2}) \quad (5b)$$

Equation 5a denotes the regression for partially cloud covered scenes whereas Equation 5b represents the optimization for fully covered cases. The coefficients a_i are dependent on the required flux density type, whereas the exponents b and c remain constant through the PAR wavelength ranges. In Table 2 the statistics of the retrievals for the three wavelength bands are presented. The standard errors of the retrievals for cloudfree scenes are below 5 Wm^{-2} due to the dominant dependence upon the sun zenith angle. Variations in the surface albedo, ozone concentration, and aerosol content contribute less effectively. For larger aerosol loadings of the atmosphere, the given relations would become inaccurate because the particle backscatter then increases rapidly. Frouin *et al.* (1989) have shown that the PAR irradiance could be changed by 10 percent by extreme differences in the visibility as a function of aerosol contents. This, however, only becomes important for continental aerosol conditions. A comparison with their model for cloudfree PAR estimates for the 350- to 700-nm and 400- to 700-nm intervals has shown deviations less than 10 Wm^{-2} . Our model generally produced higher values of PAR irradiances due to the low aerosol concentrations which have been used for marine environments.

Figure 2 shows the scatter in the comparison of the simulated (real) and the retrieved values of PAR net flux densities. The standard errors for cloudy cases are generally less than 35 Wm^{-2} (Table 2). This error is a result of the fractional cloud coverage, which complicates the relation between the geometrical extent of the cloud and the solar geometry. Both the clear sky and the cloudy part of the radiation components in a single cloud layer interact with both parts of the aligned layers, so that the sum of direct and diffuse radiation is not simply a linear function of the fractional coverage, C . Thus, for extreme variations in cloud coverage and density or large sun zenith angles, the errors are increased. For fractional coverages with $C=1$, the errors increase because the depression of the cloud transmission is strong with increasing cloud depth, so that the nonlinearity in the albedo-irradiance relationship is enhanced.

A direct estimation of PAR flux densities by the use of the corresponding PAR albedos, instead of the albedos in the spectral range of the satellite radiometer, leads to standard errors below 20 Wm^{-2} because of the spectral dependence of the atmospheric transmittance and reflectance. Thus, the

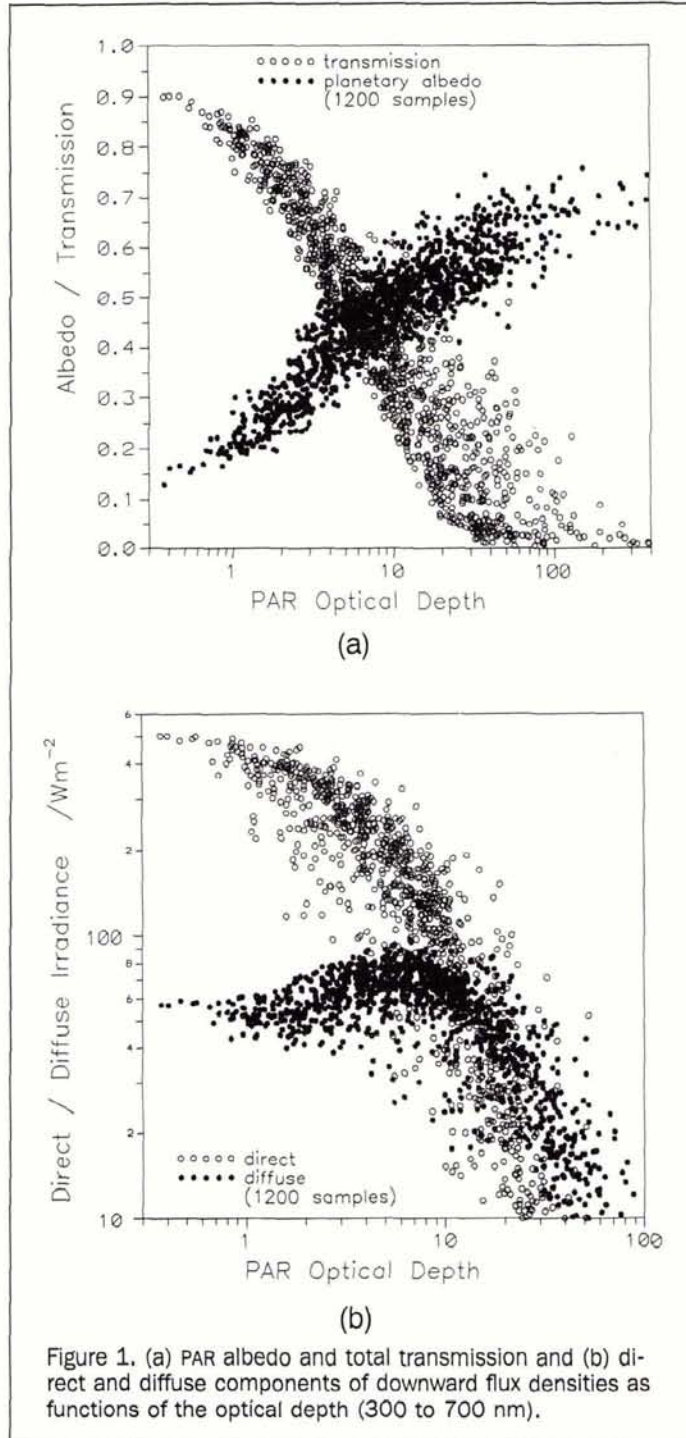


Figure 1. (a) PAR albedo and total transmission and (b) direct and diffuse components of downward flux densities as functions of the optical depth (300 to 700 nm).

TABLE 2. STANDARD ERRORS OF THE RETRIEVALS FROM EQUATIONS 4 AND 5.

Parameter	Standard Errors		
	300-700 nm	350-700 nm	400-700 nm
<i>cloudfree:</i>			
$F_{PAR,net}$	4.3/3.2 Wm^{-2}	3.7/2.4 Wm^{-2}	3.2/1.8 Wm^{-2}
F_{PAR}	3.4/3.4 Wm^{-2}	2.6/2.6 Wm^{-2}	1.9/1.9 Wm^{-2}
<i>partially cloud covered:</i>			
$F_{PAR,net}$	34.7 Wm^{-2}	32.2 Wm^{-2}	29.7 Wm^{-2}
F_{PAR}	37.2 Wm^{-2}	35.4 Wm^{-2}	33.1 Wm^{-2}
<i>fully cloud covered:</i>			
$F_{PAR,net}$	43.7 Wm^{-2}	38.2 Wm^{-2}	34.6 Wm^{-2}
F_{PAR}	46.4 Wm^{-2}	46.5 Wm^{-2}	41.2 Wm^{-2}

above standard errors include both the statistical errors of the multivariate parameters and the uncertainties of the spectral relation, i.e., the wavelength band conversion contributes by approximately 40 percent to the tabulated total errors.

Results

In principle, the algorithms are applicable to all sensors which measure the bidirectional reflectivity of the Earth-atmosphere system at the top of the atmosphere between 500 and 700 nm. In this study, satellite data of the AVHRR channel 1 with a spectral sensitivity between 550 nm and 760 nm onboard NOAA-10 and -11 was used. The deviation in the spectral bands of these sensors and the retrieval albedo ρ^* was neglected due to the fact that the albedo as a dimensionless value was used instead of radiation flux densities, so that the width of spectral bands is meaningless as far as the radiative processes over both the simulated and real sensor bands are the same (e.g., the water vapor absorption which becomes effective at wavelengths above 760 nm).

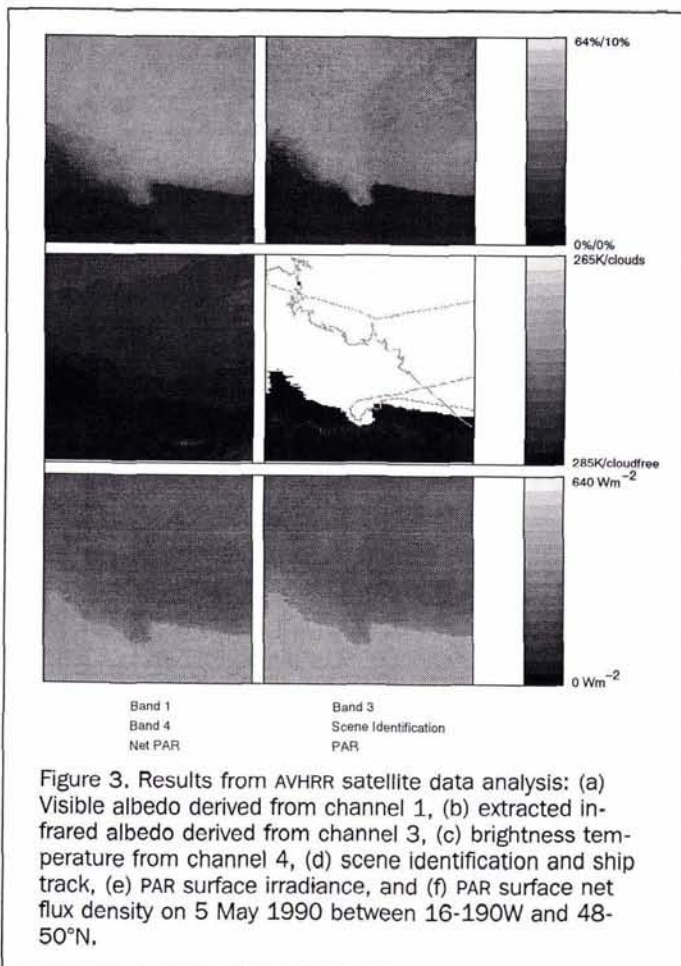
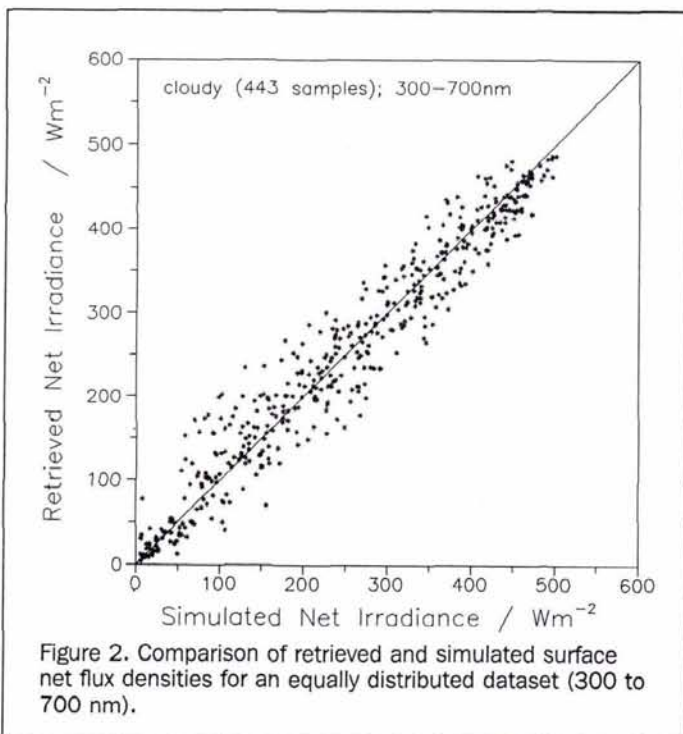
The raw data were calibrated (Lauritson *et al.*, 1979) and geographically located (Klokocnik *et al.*, 1991). The channel 1 counts were calibrated to the bidirectional target reflectivity, which was then normalized to normal illumination. The hemispherical albedo was computed by application of the scene dependent anisotropy correction factors of Taylor and Stowe (1984), which have been derived for the NIMBUS-7 ERB instrument. These factors are principally designed for the entire solar spectrum, but at present, no further alternative is available. The data from channels 3 and 4 were used for the cloud discrimination. The use of the third channel is critical because its spectral sensitivity (3440 to 4050 nm) includes both reflected solar and emitted thermal radiation of the target. The separation of the solar part of channel 3 followed Raschke *et al.* (1986). Assuming that the emissivity of clouds is equal in the spectral bands of channel 3 and 4 of the AVHRR, the thermal contribution to channel 3 is subtracted

from the total radiance, L , by applying the filtered planck response function of channel 3 to channel 4 brightness temperatures, because the latter has no solar contribution: i.e.,

$$\Delta L_{Ch3} = L_{Ch3} - B_{Ch3}(T_{Ch4}). \quad (6)$$

The difference ΔL_{Ch3} was converted to an albedo by a division by the sum of the solar irradiance in this wavelength band. This separation allows a proper discrimination of water clouds over water and snow/ice surfaces because droplets scatter effectively in this spectral region in contrast to ice and water which are nearly non-reflective. For shorter wavelengths, the effect of aerosol backscatter and roughened water reflections for higher solar zenith angles can be problematic for the distinction of thin clouds. The planetary albedo of clear scenes could reach values of 0.3, which is equal to the albedo of fog or thin clouds. In the infrared bands of the AVHRR, the occurrence of thin and low level clouds arouse the same problems, although these bands are more suitable for cloud discrimination. Clouds were identified for channel 3 albedos above 0.03 and channel 4 brightness temperatures below 278 K. The threshold of the temperature was arbitrarily chosen due to the generally constant surface conditions during the measurement period of the surface data in May 1990.

In Figures 3 and 4, examples for the multispectral satellite measurements and the above described algorithms are presented for two different situations. The first shows a stratiform cloud system during a frontal overpass, in contrast to vertically extended and spatially varying cloud structures



with strong gradients in both albedo and temperature given in Figure 4. The cloud reflectivities in Figure 3 are mainly homogeneous with values close to 0.5 (50 percent) and cloud top temperatures between 275 K and 280 K, which is typical for low level marine stratus. The corresponding PAR irradiances at the surface show amounts between 200 Wm^{-2} and 250 Wm^{-2} with few spatial variations. Figure 4 presents more inhomogeneously distributed PAR amounts due to few cloudfree parts and two diagonal bands of very dense clouds with cold cloud tops. The cloud albedos reach values above 0.6 (60 percent) and the temperatures decrease to below 250 K due to larger cloud thicknesses, which results in much lower PAR amounts with minimum values below 50 Wm^{-2} . The brightening at cloud edges is problematic because it is not automatically identifiable, which leads to a systematic underestimation of the surface flux densities whereas shadows produce overestimations.

The experimental data have been recorded during the British Ocean Flux Study (BOFS) cruise of the research vessel Charles Darwin through the North Atlantic in May 1990. The cruise site was located between 48°N - 50°N and 16°W - 19°W . The ship drifted in a south-eastward direction following the fields of highest plankton concentrations. The ship track is marked in Figures 3d and 4d. Apart from the biological data, PAR irradiances were measured at 30-second intervals.

The port and starboard values were merged to avoid shading effects as much as possible. The data have been smoothed by running averages over 5 minutes. For the collocation of ship and satellite measurements in time, the ship data have been linearly interpolated to the satellite overpass times. To reduce the errors due to the satellite geocoding procedure and the different sampling characteristics of the shipborne and spaceborne measurements, the satellite irradiance values were derived by a weighted average over 5- by 5-pixel matrices. The bounded values were weighted by the in-

verted square of their distance from the center of the matrix. The standard deviations in these sums show values above 30 Wm^{-2} , which indicates the difficulties in collocating approximately simultaneous measurements. The shipboard measurements were recalibrated to the spectral range of the satellite estimations. The resulting root-mean-square error for the satellite estimations is below 50 Wm^{-2} which is approximately equal to the standard errors of the retrievals. The satellite estimates are generally lower (ca. 20 Wm^{-2}) for cloudfree conditions and higher (50 Wm^{-2}) for cloud covered scenes because of the different spectral ranges of the estimates and the measurements. The shipborne measurements are affected by droplet absorption due to the spectral sensitivity of the radiometers above 750 nm. Thus, the PAR transmission is underestimated, resulting in lower amounts of the irradiance. The comparison indicates the high accuracy of the presented algorithms for varying atmospheric and cloud conditions, although the data set of this case study is not large enough to prove their global applicability. The differences between the results of the algorithm dedicated to partially cloud covered situations and that to fully covered scenes are small except for very dense clouds where the latter produces lower values of surface irradiances. For average conditions, i.e., for cloud transmittances between 0.8 and 0.4, the differences of both are below 20 Wm^{-2} . Thus, for satellite radiometers with high spatial resolution, the algorithm for complete coverage should be preferred and, for increasing areal means, the other would give better results.

Phytoplankton Growth Model

We are currently modeling the exceptional phytoplankton blooms in the mid north Atlantic. To do this we have studied ordinary differential equation (ODE) models published by Fasham *et al.* (1990) and Marra and Ho (1992) of the local dynamics of, variously, the phytoplankton, phytoplankton photosynthesis quota, zooplankton, bacteria, detritus, nitrate, nitrite, and ammonia. These local ODE models have to be spatially extended to a two-dimensional partial differential equation (PDE) model of the mid north Atlantic roughly situated around 48°N - 50°N and 16°W - 19°W . In order to extend the local ODE model to a PDE of any reasonable accuracy, we have kept the number of dimensions in the ODE to a minimum, by using the following grossly simplified model of phytoplankton, zooplankton, and "nutrients":

$$dN/dt = f_N(N, P, Z, F_{PAR,net}), \quad (7a)$$

$$dP/dt = f_P(N, P, Z, F_{PAR,net}), \quad (7b)$$

$$dZ/dt = f_Z(N, P, Z, F_{PAR,net}) \quad (7c)$$

$$dN/dt = m_p P + m_z Z - P_{max} [F_{PAR,net} N / (K_{PAR} + F_{PAR,net}) (K_N + N)] P - D(N - N_o) - SN \quad (8a)$$

$$dP/dt = P_{max} [F_{PAR,net} N / (K_{PAR} + F_{PAR,net}) (K_N + N)] P - m_p P - gPZ \quad (8b)$$

$$dZ/dt = gPZ - m_z Z \quad (8c)$$

where P_{max} , K_{PAR} , and K_N represent the maximum and half saturation constants of a Michaelis-Menton saturation for photosynthetically available radiation ($F_{PAR,net}$) and nutrients, respectively; g denotes the rate of grazing of phytoplankton by zooplankton; m_p and m_z represent the mortality rates of the phytoplankton and zooplankton, respectively; D denotes the rate of diffusion of nutrients between the well mixed layer and the deep layer; N_o denotes the concentration of nutrients in the deep layer; and S denotes the rate at which nutrients settle (sink) out of the well mixed layer into the deep layer. For this model we have exhaustively searched the pa-

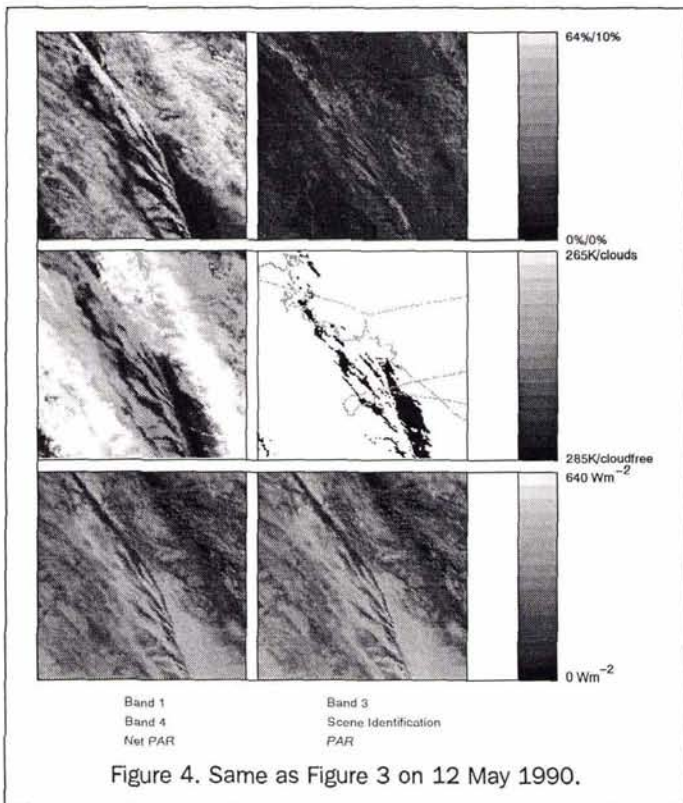


Figure 4. Same as Figure 3 on 12 May 1990.

parameter space for parameter values for the local dynamical model which we feel best reflect the regional biology. In our local ODE model, the phytoplankton represent the bottom of the local food chain. They are the primary producers of the food required to support the major part of the zooplankton and bacterial populations. One of the most important "external" parameters of our local ODE model is the amount of PAR used by the phytoplankton for metabolism. Assuming that the nutrients, phytoplankton, and zooplankton are all passively convected by the ocean currents, our spatially extended PDE model consists of the following convective reaction diffusion equation:

$$dN/dt = f_N(N, P, Z, F_{PAR,net}) + (\delta/\delta x, \delta/\delta y) (D_N(\delta/\delta x, \delta/\delta y)N - Nv) \quad (9a)$$

$$dP/dt = f_P(N, P, Z, F_{PAR,net}) + (\delta/\delta x, \delta/\delta y) (D_P(\delta/\delta x, \delta/\delta y)P - Pv) \quad (9b)$$

$$dZ/dt = f_Z(N, P, Z, F_{PAR,net}) + (\delta/\delta x, \delta/\delta y) (D_Z(\delta/\delta x, \delta/\delta y)Z - Zv) \quad (9c)$$

where $(\delta/\delta x, \delta/\delta y)$ denotes the two-dimensional Del Operator, and $v = v(x, y, t)$ is the velocity vector of the ocean fluid flow. Note that, in this PDE model, the internal variables, $N = N(x, y, t)$, $P = P(x, y, t)$, and $Z = Z(x, y, t)$ as well as the external variables $F_{PAR,net} = F_{PAR,net}(x, y, t)$ and $v = v(x, y, t)$ are all functions of space, x , y , and time, t . In order to numerically integrate the PDE model, we require knowledge of the values of the internal variables at time $t = 0$ over the whole spatial domain of interest. We also require knowledge of the external variables over the whole of both the spatial domain and the time interval of interest. While we can only use satellite images to infer the velocity field, $v(x, y, t)$, we can use the regressive model outlined in the first part of this paper to calculate the PAR field (PAR map), $F_{PAR,net}(x, y, t)$, throughout the time interval of interest.

Ideally, we would like to calculate PAR maps often enough to use them as the boundary condition, $F_{PAR,net}(x, y, t)$, in the numerical integration of our PDE model. Unfortunately, we have not been able, as yet, to obtain enough images to make this practical. To do this we would, ideally, require an image every half hour for about 5 years. While this is currently "possible" for a geostationary satellite, it is prohibitively expensive. The creation of large but incomplete numbers of PAR maps from remotely sensed satellite images can still assist our modeling in two ways. First, such a collection of PAR maps allows us to qualitatively determine how much PAR was supplied to phytoplankton at around the time of the bloom. We can also qualitatively determine how important the variability in the PAR was for the initiation of the bloom.

Second, such a collection of PAR and associated cloud maps is also useful to accurately determine the mean and variance of the PAR to which the phytoplankton are exposed. In particular, we have used our existing collection of PAR maps to determine the probabilities of changing from very cloudy to slightly clouded conditions and vice versa. Using these probabilities, we have constructed a spatially extended stochastic (Markovian) model of the PAR available to the mid north Atlantic ecosystem. We are using this a model to calculate a first order approximation to boundary condition, $F_{PAR,net}(x, y, t)$, required for the numerical integration of our spatially extended PDE model of a phytoplankton bloom.

Concluding Remarks

New regression algorithms have been derived to estimate the PAR surface and net flux densities over sea surfaces from satellite measurements in the visible wavelength range. The

regressions are applicable to three most commonly used PAR intervals, and show standard errors between 30 and 40 Wm^{-2} , which is confirmed by an application case study during a shipborne experiment in the North Atlantic in 1990. The largest errors occurred due to the inhomogeneous reflection characteristics of three-dimensional clouds which could partly be reduced by spatial averaging. The simplicity of the algorithms and their direct application to appropriate satellite measurements from both polar orbiting and geostationary platforms potentially may provide an effective tool to biological applications.

The potential use of instantaneously calculated PAR charts is demonstrated by the formulation of a two-dimensional phytoplankton growth model. The real energy supply provided by the satellite estimates over space and time could improve the determination of the interdependence between PAR and growth, e.g., blooms, with respect to other limiting factors.

Acknowledgments

We gratefully thank the National Environment Research Council (NERC) for making the shipboard and satellite data available.

References

- Bishop, J.K.B., and W.B. Rossow, 1991. Spatial and Temporal Variability of Global Surface Irradiance, *J. Geophys. Res.*, 96(C9):16.839-16.858.
- Coakley, J.A., R.D. Cess, and F.B. Yurevich, 1983. The Effect of Tropospheric Aerosols on the Earth's Radiation Budget: A Parameterization for Climate Models, *J. Atmos. Sci.*, 40:116-138.
- Eck, T.F., and D.G. Dye, 1991. Satellite Estimation of Incident Photosynthetically Active Radiation Using Ultraviolet Reflectance, *Remote Sens. Environ.*, 36:135-146.
- Fasham, J.R., H.W. Ducklow, and S.M. McKelvie, 1990. A Nitrogen-Based Model of Plankton Dynamics in the Oceanic Mixed Layer, *J. Marine Res.*, 48:591-639.
- Frouin, R., D.W. Lingner, C. Gautier, K.S. Baker, and R. Smith, 1989. A Simple Analytical Formula to Compute Clear Sky Total and Photosynthetically Available Solar Irradiance at the Ocean Surface, *J. Geophys. Res.*, 94(C7):9.731-9.742.
- Green, A.E.S., 1964. Attenuation by Ozone and the Earth's Albedo in the Middle Ultraviolet, *Appl. Opt.*, 3:203-208.
- Jitts, H.R., A. Morel, and Y. Saijo, 1976. The Relation of Oceanic Primary Production to Available Photosynthetic Radiation, *Aust. J. Mar. Freshwater Res.*, 27:441-454.
- Joseph, J.J., W.J. Wiscombe, and J.A. Weinman, 1976. The Delta-Ed-dington Approximation for Radiative Flux Transfer, *J. Atmos. Sci.*, 33:2.452-2.459.
- Klokocnik, J., P. Schlüssel, J. Kosteletzky, and H. Grassl, 1991. *On the Navigation of Polar Orbiting Meteorological Satellites*, Report No. 75, MPI of Meteorology.
- Lacis, A., and J.E. Hansen, 1974. A Parameterization for the Absorption of Solar Radiation in the Earth's Atmosphere, *J. Atmos. Sci.*, 31:119-133.
- Lauritson, L., G.J. Neslon, and F.W. Porto, 1979. *Data Extraction and Calibration of TIROS-N / NOAA Radiometers*, NOAA Tech. Mem., NESS 107.
- Margraff, W.A., and M. Griggs, 1969. Aircraft Measurements and Calculations of the Total Downward Flux of Solar Radiation as a Function of Altitude, *J. Atmos. Sci.*, 26:798-805.
- Marra, J., and C. Ho, 1992. Initiation of the Spring Bloom in the Northeast Atlantic (47°N / 20°W): A Numerical Simulation, *Deep Sea Res.*, in press.
- Platt, T., W.G. Harrison, M.R. Lewis, W.K.W. Li, S. Sathyendranath, R.E. Smith, and A.F. Vezina, 1989. Biological Production of the Oceans: The Case for a Consensus, *Mar. Ecol. Progr. Ser.*, 52:77-88.

Raschke, E., H. Jacobs, H.J. Lutz, and U. Steffens, 1986. Wolkenerkennung über der Antarktis in Satellitenbildern, *Polarforschung*, 56:69-78.

Sathyendranath, S., and T. Platt, 1988. The Spectral Irradiance Field at the Surface and in the Interior of the Ocean: A Model for Applications in Oceanography and Remote Sensing, *J. Geophys. Res.*, 93:9270-9280.

Silverman, B.A., and E.D. Sprague, 1970. Airborne Measurements of

In-Cloud Visibility, *Nat. Conf. on Weather Modif.*, AMS, Santa Barbara, California.

Taylor, V.R., and L.L. Stowe, 1984. Reflectance Characteristics of Uniform Earth and Cloud Surfaces Derived from NIMBUS-7 ERB, *J. Geophys. Res.*, 89(D4):4.987-4.996.

Zdankowski, W.G., W.G. Panhans, R.M. Welch, and G. Korb, 1980. A Radiation Scheme for Circulation and Climate Models, *Contr. to Atmos. Phys.*, 55:215-238.

Introduction to the PHYSICS AND TECHNIQUES OF REMOTE SENSING

by: Charles Elachi

Introduction to Physics and Techniques of Remote Sensing is a comprehensive overview of the basics behind remote-sensing physics, techniques, and technology. Elachi details the basic physics of wave/matter interactions, techniques of remote sensing across the electromagnetic spectrum (UV, visible, infrared, mm, and microwave), and the concepts behind current remote sensing techniques and future ones in development. Applications of remote sensing are described for a wide spectrum of earth and planetary atmosphere and surface sciences, including geology, oceanography, resource observation and atmospheric sciences, and ionospheric studies.

This book provides the basic scientific and engineering background for students and researchers interested in remote sensing and its applications. The text is self-comprehensive and requires the reader to have the equivalent of a junior-level in physics, specifically introductory electromagnetic and quantum theory.

Chapters include:

- Introduction
- Nature and Properties of Electromagnetic Waves
- Solid-Surfaces Sensing in the Visible and Near Infrared
- Solid-Surfaces Sensing: Thermal Infrared
- Solid-Surface Sensing: Microwave Emission
- Solid-Surface Sensing: Microwave and Radio Frequencies
- Ocean Surface Sensing
- Basic Principles of Atmospheric Sensing and Radiative Transfer
- Atmospheric Remote Sensing in the Microwave Region
- Millimeter and Submillimeter Sensing of Atmospheres
- Atmospheric Remote Sensing in the Visible and Infrared
- Ionospheric Sensing

1987. 413 pp. 17 colorplates. \$75 (hardcover); ASPRS Members \$57. Stock # 4529.

For ordering information, see the ASPRS Store in the back of this journal.